NANO · MICRO small
www.small-journal.com

Flexible Nanoarchitectonics for Biosensing and Physiological Monitoring Applications

Aditya Ashok, Tuan-Khoa Nguyen, Matthew Barton, Michael Leitch, Mostafa Kamal Masud,* Hyeongyu Park, Thanh-An Truong, Yusuf Valentino Kaneti, Hang Thu Ta, Xiaopeng Li, Kang Liang, Thanh Nho Do, Chun-Hui Wang, Nam-Trung Nguyen, Yusuke Yamauchi,* and Hoang-Phuong Phan**

Flexible and implantable electronics hold tremendous promises for advanced healthcare applications, especially for physiological neural recording and modulations. Key requirements in neural interfaces include miniature dimensions for spatial physiological mapping and low impedance for recognizing small biopotential signals. Herein, a bottom-up mesoporous formation technique and a top-down microlithography process are integrated to create flexible and low-impedance mesoporous gold (Au) electrodes for biosensing and bioimplant applications. The mesoporous architectures developed on a thin and soft polymeric substrate provide excellent mechanical flexibility and stable electrical characteristics capable of sustaining multiple bending cycles. The large surface areas formed within the mesoporous network allow for high current density transfer in standard electrolytes, highly suitable for biological sensing applications as demonstrated in glucose sensors with an excellent detection limit of 1.95 µM and high sensitivity of 6.1 mA cm^{-2} $µM^{-1}$, which is approximately six times higher than that of benchmarking flat/non-porous films. The low impedance of less than 1 kΩ at 1 kHz in the as-synthesized mesoporous electrodes, along with their mechanical flexibility and durability, offer peripheral nerve recording functionalities that are successfully demonstrated in vivo. These features highlight the new possibilities of our novel flexible nanoarchitectonics for neuronal recording and modulation applications.

1. Introduction

Implantable biomedical devices provide powerful tools for diagnosing and treating several chronic diseases that have saved millions of lives and significantly improved individuals' quality of life.[1–3] Well-known examples include cardiac pacemakers that enable the regulation of the heart rate and rhythm[4] and cochlear implants that provide sound perception to patients with sensorineural hearing loss.[5] Introducing functional electronics with physiological recording and stimulation capabilities has also created an untraditional pathway for treating nervous system disorders such as Parkinson's disease and spinal cord injuries.[6] Although modern implanted electronics have witnessed rapid development over the past 6 decades, most commercially available devices are still built on relatively similar designs concept consisting of a thick ceramic housing for electronics encapsulation and long metallic wires for biological tissue

A. Ashok, M. K. Masud, H. Park, Y. V. Kaneti, Y. Yamauchi, H.-P. Phan
Australian Institute of Bioengineering and Nanotechnology
The University of Queensland
St Lucia, Queensland 4067, Australia
E-mail: m.masud@uq.edu.au; y.yamauchi@uq.edu.au; hp.phan@unsw.edu.au

A. Ashok, T.-K. Nguyen, T.-A. Truong, H. T. Ta, N.-T. Nguyen, H.-P. Phan
Queensland Micro and Nanotechnology Centre
Griffith University
Nathan, Queensland 4111, Australia
E-mail: k.nguyentuan@griffith.edu.au

The ORCID identification number(s) for the author(s) of this article can be found under https://doi.org/10.1002/smll.202204946.

DOI: 10.1002/smll.202204946

M. Barton, M. Leitch
School of Nursing and Midwifery
Griffith University
Southport, Queensland 4215, Australia

M. Barton
Menzies Health Institute Queensland – Griffith University
Southport, Queensland 4215, Australia

T.-A. Truong, X. Li, C.-H. Wang, H.-P. Phan
School of Mechanical and Manufacturing Engineering
The University of New South Wales
Sydney, New South Wales 2052, Australia

K. Liang, T. N. Do
Graduate School of Biomedical Engineering
The University of New South Wales
Sydney, New South Wales 2052, Australia

K. Liang
School of Chemical Engineering
The University of New South Wales
Sydney, New South Wales 2052, Australia

interfaces.[7,8] The use of thick ceramic or titanium packaging allows for relatively long-term stable operation; however, the mechanical mismatch between the implanted components and the soft nature of biological tissue poses potential risks to users and limits functional modalities.[9] Recent advancements in material science have accelerated the research into flexible electronics platforms, creating exciting opportunities for the seamless integration of electronics into tissues.[10–12] For instance, silicon nanomembrane transistors transferred from standard bulk wafers onto polymeric substrates can conform to the curvilinear surface of the heart and record cardio physiological signals over a large surface area.[13] Flexible organic material-based electrode arrays were successfully demonstrated to record action potentials from superficial cortical neurons that potentially facilitate minimally invasive diagnoses and treatments for brain disorders.[14]

An essential requirement of implanted devices is the low impedance at the electronic-tissue interface to enable the detection of relatively low biopotentials, which typically fall within a range of a few microvolts.[15,16] In addition, to decipher the functionalities of complex neural circuits, high-density and high-resolution miniaturized electrode arrays distributed on a soft, planar substrate are desired.[17,18] As the dimension of electrodes is shrunk to a sub-hundred micrometer scale, the small surface areas generally lead to an increase in the electrochemical impedance. This causes a significant reduction in the signal-to-noise ratio (S/N) in the physiological recording. Diminution in the active Faradaic interface also decreases the charge injection capacity (CIC) or charge storage capacity (CSC), hindering the effectiveness of implanted stimulation electrodes. To overcome these limitations, several approaches have been proposed to engineer (increase) the effective surface areas of electrodes and subsequently reduce their electrochemical impedance. For instance, stacking numerous layers of nanoflakes or nanopores of highly conductive 2D materials such as graphene[19–22] and graphene oxide[23,24] can significantly minimize impedance. Spin-coating or drop-casting a network of metallic nanowires or carbon nanotubes can also increase the effective surface areas, thereby enhancing the impedance spectra of electrodes.[25–29] However, the unstable physical attachment of these nanoarchitectures (e.g., nanoflakes, nanowires and/or nanodots) onto conductive surfaces could lead to problems in material uniformity, deposition selectivity, delamination, and scalability for mass-manufacturing. Alternative methods using top-down fabrication techniques to create high-density nanoholes on metallic materials can enhance the surface area along with well-controlled uniformity.[30–32] These methods of developing small-sized nanopores require sophisticated equipment such as electron beam lithography or focused ion beam, typically increasing the processing time and device costs. Other top-down techniques, such as laser-reduced graphene oxide, have been developed to form microelectrodes for chemical and biosensing applications.[33] Since the fabrication process involves high-power laser irradiation, achieving high-resolution devices and integration with other functioning components that are sensitive to temperature are difficult. In addition, drop casting is another common method to deposit nanostructured materials on different templates. For example, graphene oxide decorated with a metal–organic framework has been employed for NO_2 gas sensors.[34] However, material uniformity, fabrication scalability, and the physical bonding between the functioning elements and the substrate have been challenging issues in this approach.

We have recently successfully developed a variety of mesoporous materials, which cover a wide range of materials from metals to semiconductors.[35–38] The porous network within these materials can significantly boost the overall performance of functional devices because of the significantly increased surface area. Some unique features offered by the mesoporous architecture include a high absorption spectrum for optoelectronics, excellent electrochemical properties for biosensing, and the capability of loading and releasing biomaterials for drug delivery. Despite these significant merits, the current mesoporous materials are mainly synthesized on rigid conductive substrates such as indium tin oxide (ITO) and metal-coated silicon substrates. This limits their potential for flexible electronics applications, particularly implemented biomedical applications. To address these issues, in this work we introduce a new engineering pathway that combines top-down and bottom-up methods to selectively synthesize flexible mesoporous metallic gold (MP-Au) films as electrodes for biosensing and bioimplant applications. Taking advantage of mesoporous materials and advanced microlithography, the proposed platform exhibits a low electrochemical impedance, excellent mechanical deformability, and capability for physiological recording verified through an *in vivo* study on an animal model. The results confirm that our approach offers a new route toward miniaturization, high density of nanoarchitectured electrodes for implanted *in vivo* medical devices that can support both fundamental neuroscience investigation and clinical applications.

T. N. Do, H.-P. Phan
Tyree Foundation Institute of Health Engineering
The University of New South Wales
Sydney, New South Wales 2052, Australia
Y. Yamauchi
School of Chemical Engineering
The University of Queensland
St Lucia, Queensland 4067, Australia
Y. Yamauchi
JST-ERATO Yamauchi Materials Space-Tectonics Project and International Center for Materials Nanoarchitectonics (WPI-MANA)
National Institute for Materials Science
Tsukuba, Ibaraki 305-0044, Japan

2. Results and Discussion

2.1. Fabrication Route for Flexible Mesoporous Au Electrodes

The demand for a simple and robust fabrication process of conductive mesoporous architectures toward flexible electronics is enormous. We demonstrate here a hybrid fabrication process combining both the top-down micro electromechanical system (MEMS) micromachining and bottom-up electrochemical deposition to realize flexible metallic mesoporous electrodes (**Figure 1**a). In the present experiment, a Ti/Au (20/200 nm)

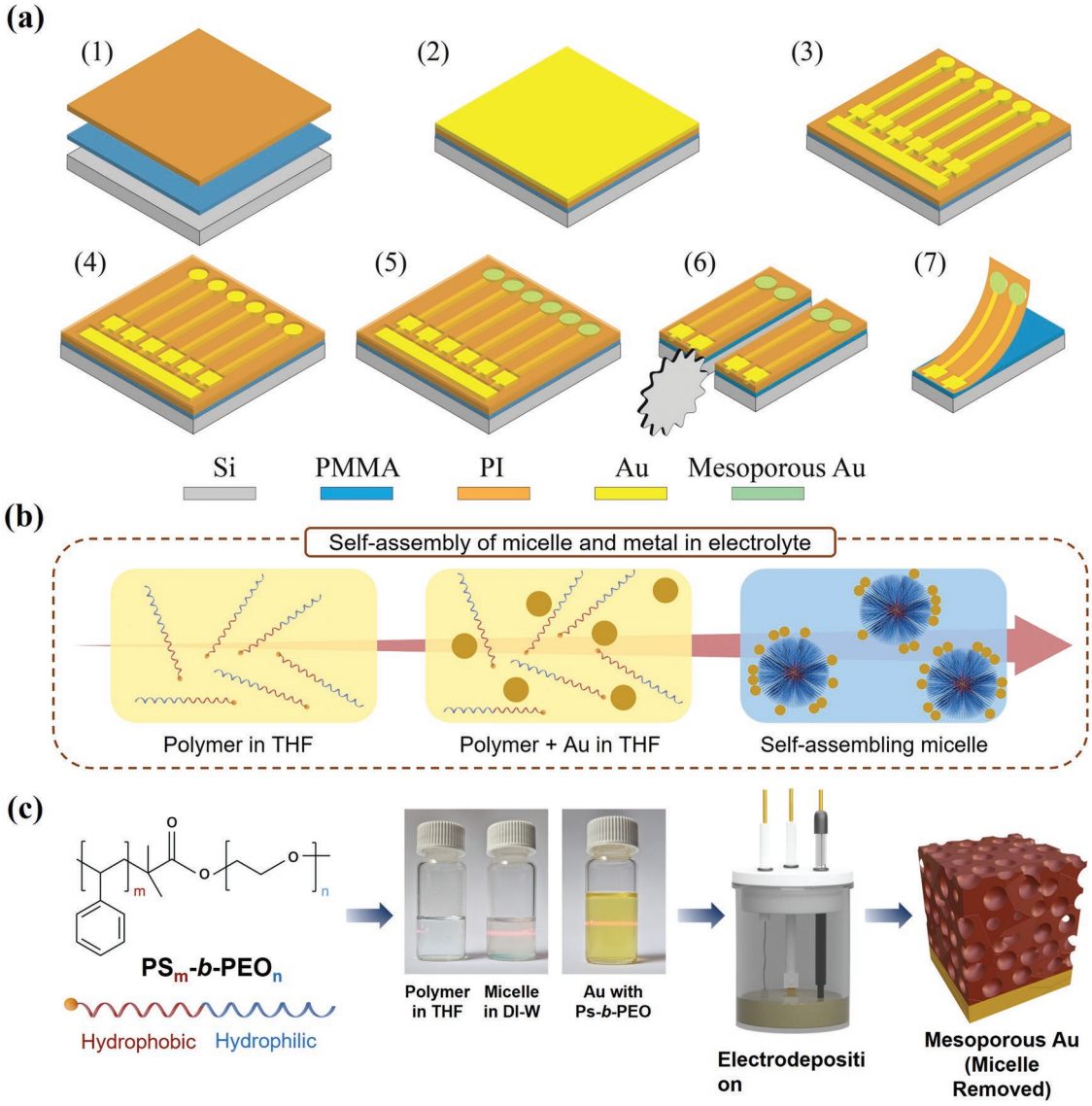

Figure 1. Concept of flexible mesoporous metallic gold (MP-Au). a) Schematic sketch of the MP-Au array and fabrication process. b) Concept of the self-assembly of polymeric micelles with metal species. c) Electrochemical deposition process to form mesoporous conductive networks.

thin film deposited on a polyimide (PI) substrate served as the seed layer for the growth of the mesoporous layer. Polyimide was selected as the flexible substrate due to its mechanical flexibility and chemical stability that well tolerates the subsequent electrochemical deposition of mesoporous Au. A thin Au film was patterned into microelectrodes with active sizes of 60 µm in diameter using standard lithography and metal wet etching. Spin-coating and patterning another 3 µm-thick PI film on the Au electrodes provided an encapsulation layer, with the opening windows designed at the active area. A three-electrode system with a Pt counter electrode and an Ag/AgCl reference electrode was applied to selectively grow mesoporous Au onto the opening windows. The electrolyte for electrodeposition of mesoporus Au contained Au species (dissolved in ddH_2O) and PS(10k)-*b*-PEO(4.1k) diblock co-polymers (in THF) (the number indicates the molecular weight for each block). The micellization of diblock co-polymers occurred by adding water, accessed by observing laser beam scattering on the (Figure 1b). The applied deposition potential was fixed for mesoporous Au at –0.5 V (vs. Ag/AgCl), as optimized in our previous studies on a rigid substrate.[35] By connecting all active electrodes to the common working electrode terminal, we enabled the selective and simultaneous deposition of mesoporous architecture on the seeding layer. These connection paths were then removed using wafer dicing, allowing MP-Au electrodes to function separately. The capability of simultaneous deposition of MP-Au on several targeted sites makes the proposed hybrid technique highly feasible for wafer-level fabrications. The step-by-step fabrication process of the flexible MP-Au is further detailed in Supporting Information.

Figure 2a–c shows photographs of micro Au electrodes fabricated on a 4-inch silicon wafer with the opening areas (60 µm in diameter) well aligned with the active sites of the electrodes. The compatibility of our fabrication route with

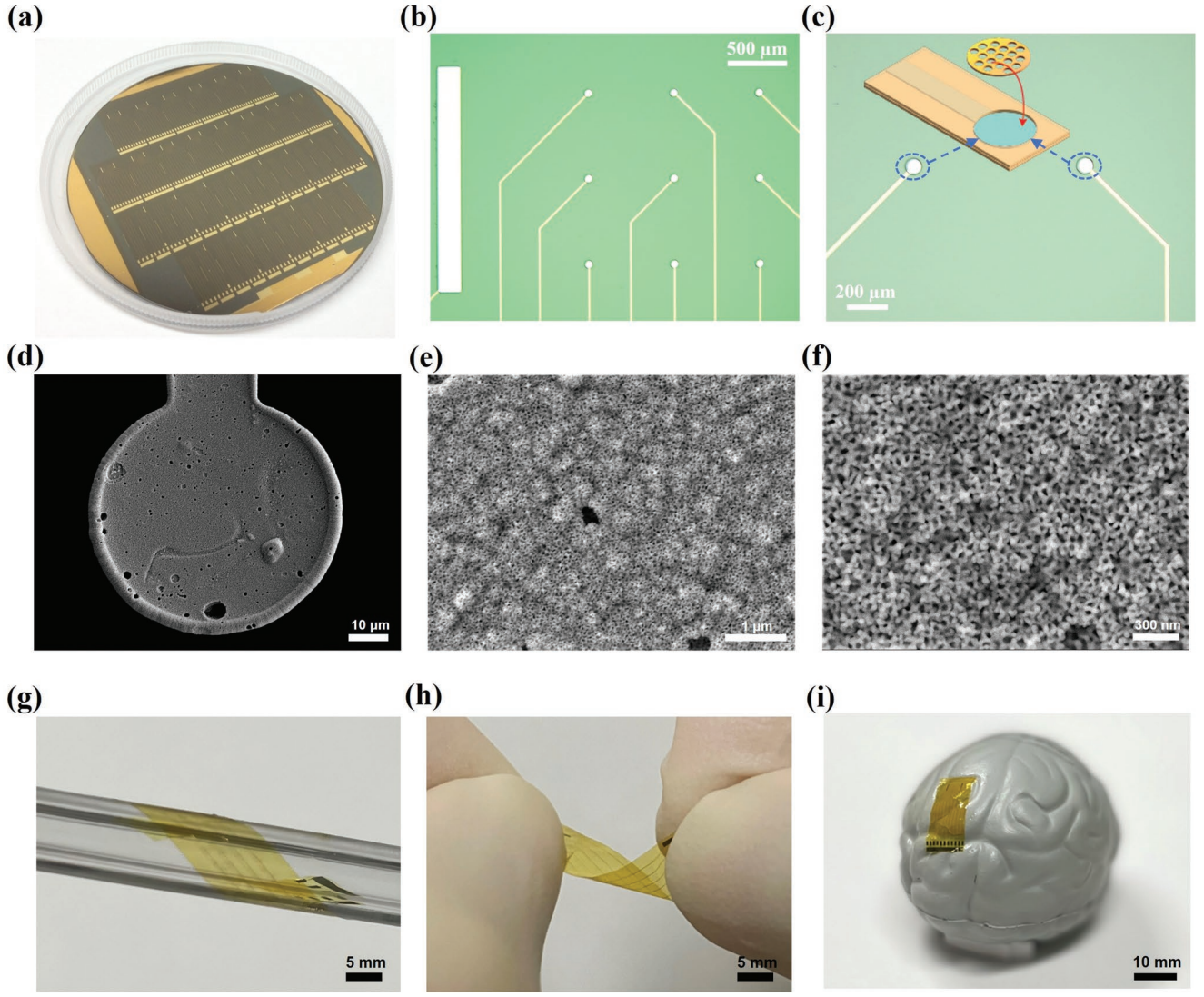

Figure 2. Photograph of micropatterned electrodes. a) Au electrodes patterned onto a full-scale wafer. b) Optical microscope image of Au microelectrodes using polyimide as the encapsulation layer with an opening window of 60 µm in diameter. c) Image of the flexible MP-Au electrode after depositing porous nanoarchitectures. d–f) SEM image of the active area with mesoporous Au deposition at different magnifications. g–i) Demonstration of mechanical flexibility: bending, twisting, and wrapping on a curved surface.

the standard microlithography enables the development of high density and miniaturized electrode arrays. The presence of mesoporous architecture can simply alter the optical properties, which can be observed through optical spectroscopy, where the flexible MP-Au electrode exhibits a dark-red color due to an enhancement in light absorption and scattering capability compared to the flat film (Figure S1, Supporting Information). The Field-Emission Scanning Electron Microscopes (FE-SEM) images confirm the formation of a mesoporous Au network with relatively good uniformity, as shown in Figure 2d–f. The average pore size of mesoporous films is measured to be around 24 nm (Figure S2, Supporting Information) by using FE-SEM images. The obtained pore size falls within a comparable range with electrochemically deposited on standard rigid platforms, indicating that the substrate does not significantly influence the as-synthesized nanoarchitecture.[35,36] The crystallographic property of the film was analyzed through grazing incidence X-ray diffraction (GI-XRD). No change is detected in the crystallographic nature apart from a very small peak broadening effect observed in the MP-Au electrode, which is attributed to its pore-induced low domain size (Figure S3, Supporting Information). Based on the SEM data, it is also evident that no mesoporous structure is observed on the encapsulation layer, ensuring that the sensing and recording functionalities can occur only at the opening sites. The MP-Au on the PI substrate can be easily detached from the initial silicon wafer by immersing the samples into acetone and IPA to remove the underlying sacrificial layer (PMMA). The small bending stiffness of the polymeric substrate enables conformal contact between electrodes and curvature surfaces such as cylinder, brain model, and human skin, as shown in Figure 2g–i.

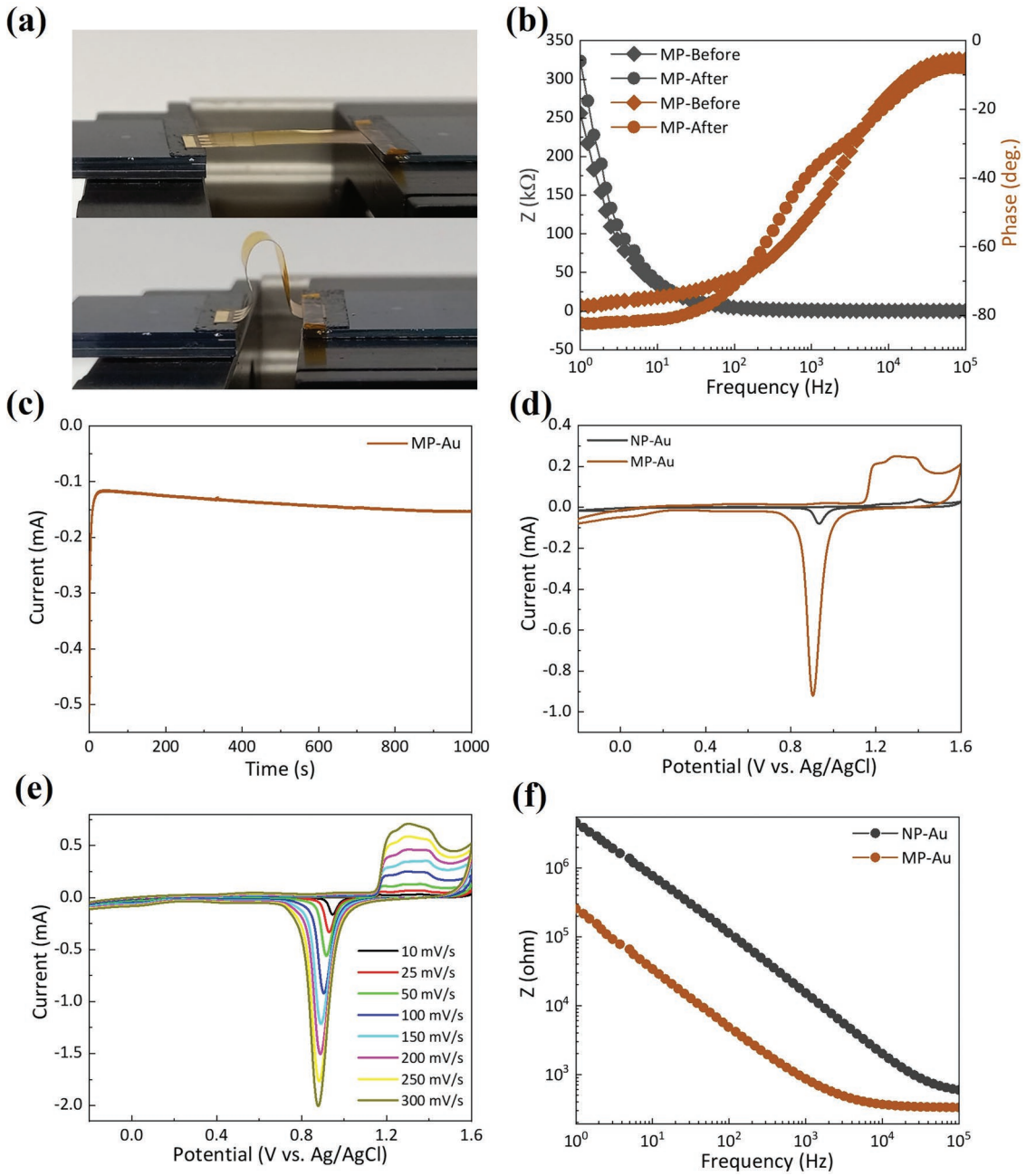

Figure 3. Electrochemical characterization of mesoporous and non-porous flexible electrodes. a) Bending test setup for investigating flexibility. b) EIS before and after the bending test. c) Chronoamperometry plot during mesoporous Au deposition on flexible substrates under –0.5 V for 1000 s (the deposition area of 2.8 nm^2). d) CV curves in 0.5 M H_2SO_4 of flat/non-porous and mesoporous Au electrode (scan rate 0.1 V s^{-1}). e) CV curves in 0.5 M H_2SO_4 for flexible MP-Au acquired at different scan rates ranging from 10 to 300 mV s^{-1}. f) EIS of flexible mesoporous gold (MP-Au) and flat/non-porous Au (NP–Au).

To further investigate the flexibility of our electrodes, a bending test using a linear actuator was carried out, as shown in **Figure 3**a and Figure S4, Supporting Information. A thousand bending cycles were applied to the MP-Au/PI, with the bending radius varying from ∞ (flat state) to 2 mm. Due to the small thickness of PI (6 µm), the distance between the functioning layer (MP-Au) to the neutral axis is only 3 µm. As a result, the maximum tensile stress induced into the Au film is estimated at a maximum of 229 MPa, which is well within the Yield stress regime of Au (see Finite Element Analysis in the Supporting Information). We further investigated the stability of electrochemical properties after 1000 bending cycles. The results presented in Figure 3b indicate stable impedance and phase characteristics in the materials, demonstrating the mechanical flexibility of our platform, suitable for bioimplant applications.

To investigate the suitability of flexible MP-Au electrodes for biosensing, a set of electrochemical measurements was

carried out including chronoamperometry, cyclic voltammetry (CV), and electrochemical impedance spectra (EIS) (Figure 3). The chronoamperometry data (Figure 3c) shows the deposition currents for the MP-Au electrode observed at a fixed potential of –0.5 V versus Ag/AgCl over a period of 1000 s. The change in the resistance causes minor fluctuations in the currents because of increasing film thickness during the deposition, indicating the formation of mesoporous thin film on the surface of the working electrode. The CV study of the as-deposited film was then performed in a 0.5 M H_2SO_4 solution and compared to the flat film counterpart. As seen in Figure 3d, the location of the reduction and oxidation (redox) peaks of MP-Au in an acidic solution is comparable to a benchmarking flat Au electrode. As such, the characteristic redox peaks are in the potential range of 0.8–1.5 V, which signifies the absorption and desorption of oxygen with respect to the Ag/AgCl reference electrode. A substantial reduction peak is observed from the CV at 0.9 V versus Ag/AgCl. Under a similar scan rate of 0.1 V s^{-1}, the current density of the flexible MP-Au electrodes is much larger than that of the non-porous (NP) NP-Au film. This significant current enhancement is attributed to the large surface areas (92.73 m^2 cm^{-3}) and interconnected porous tunnels (that provide synergistic activity) of the mesoporous film such that its effective surface area is approximately seven times higher than that of the NP-Au film (13.27 m^2 cm^{-3}). The surface area was estimated using volume normalized electrochemical surface area (ECSA). To examine the charge transport mechanism of flexible MP-Au film, CV curves were recorded at different scan rates (10–300 mVs^{-1}), which show a linear increase in both the anodic and cathodic currents (Figure 3e and Figure S5, Supporting Information). As shown in Figure S6, Supporting Information, the linear relationship between anodic/cathodic currents and the square root of the scan rate suggests the redox process in MP-Au films is diffusion-controlled and quasi-reversible.[39] Based on the CV scans, the flexible MP-Au charge specific capacity on PI is determined to be 11.39 mC cm^{-2}, approximately ten times higher than that pertinent to the NP-Au electrode (1.96 mC cm^{-2}).[40] This result is consistent with the impedance spectra recorded in the two types of electrodes, as shown in Figure 3f. Evidently, the impedance of the MP-Au film is one order of magnitude lower than that of NP–Au. This is because, the EIS represents the charge transfer between the electrode and the liquid electrolyte, which is dominated by the surface area of the electrodes. In this regard, the surface area of the NP-Au electrode is limited by its radius, whereas the MP-Au network offers a much larger surface area directly exposed to the electrolyte, which can provide a much lower EIS than the NP-Au counterpart with the same thickness. In particular, the impedance of flexible MP-Au on PI at 1 kHz is found to be 862 Ω, highly suitable for physiological recording application (e.g., within 600 kΩ). Our experimental results demonstrate that a hybrid fabrication technique that combines top-down microfabrication and bottom-up electrochemical deposition holds promise for the development of miniaturized neural electrodes with sufficiently low impedance. In addition to this better electrical performance, the flexible MP-Au is advantageous with high stability. The flexible MP-Au provides stable responses (current density) over multiple cycles (10, 20, 30 cycles) of CV measurement in phosphate-buffered saline (PBS) (Figure S7a,b,c, Supporting Information). The Nyquist plot at low impedance regime suggests a relatively lower reries resistance in the MP-Au in comparison to the non-porous electrode (Figure S7d,e, Supporting Information).

To demonstrate the advantage of the large surface areas from the porous network for biosensing applications, we employed flexible MP-Au to detect and quantify glucose levels through a glucose oxidation reaction. In a typical glucose oxidation reaction, under the specific potential glucose molecules are oxidized to gluconolactone when they encounter metal electrodes. As can be seen from **Figure 4**a (inset-right), the flexible MP-Au film undergoes a typical glucose oxidation reaction (10 mM glucose in 0.1 M PBS) and generates a high oxidation current density (≈12.9 mA cm^{-2}). The glucose oxidation peaks are observed at around 360 mV for both mesoporous and NP-Au electrodes (Figure 4a, right). However, no such oxidation peak is observed in the absence of glucose, suggesting the selective oxidation of glucose. The flexible MP-Au also attributes to the high oxidation current density (12.8 mA cm^{-2} for 10 mM glucose) compared to that of the flat/non-porous film (NP–Au) (4.43 mA cm^{-2} for 10 mM glucose) (Figure S8, Supporting Information). This is because, glucose oxidation is dependent on the exposed active sites and cascade electrocatalytic on the surface. The 3D geometry of the MP-Au electrodes provides pore-induced high surface area and more exposed active sites for glucose oxidation. Moreover, the increasing glucose concentrations from 1 µM to 50 mM results in a noticeable increase in the oxidation current densities in both electrodes (Figure 4c and Figure S9, Supporting Information), suggesting the mesoporous structure can retain and oxidize a higher level of glucose. To check the specificity and selectivity of flexible MP-Au electrode, we tested the measurement of glucose over other common interference agents, for example, ascorbic acid (AA), uric acid (UA), lactose, sucrose, fructose, and NaCl salt at a fixed concentration of 10 mM. It can be seen (Figure 4b) that the flexible MP-Au electrode generates a much higher current than that of all inferences, suggesting the applicability of flexible MP-Au for detecting glucose from a complex biological sample. For instance, the responses for AA are less than half of glucose. Moreover, after several consecutive measurements of all interferences in a single sensing electrode, the current response for glucose oxidation remains consistent with fresh/clean MP-Au electrode. This result indicates that the interferences do not significantly block the active surface of MP-Au. In the complex system such as glucose spiked in serum, the flexible MP-Au provides relatively lower current response, however it follows a similar trend to glucose in PBS (Figure S10, Supporting Information). To assess the sensitivity of flexible MP-Au as regards of the NP-Au electrode, we performed sequential chronoamperometry (CA) at different concentrations of glucose ranging from 200 nM to 1 mM. We conducted CA measurement at a low potential of 200 mV to avoid the undesired responses from unintended biomolecules (e.g., uric acid, ascorbic acid) present in the biological system, which may be prone to oxidation at a higher potential ranging from 300 to 400 mV.[35] Figure 4d shows a gradual increase in the CA current density with increasing glucose concentrations for both flexible MP-Au and NP–Au electrodes. Evidently, the larger surface area of the mesoporous architecture offers a markedly larger change in

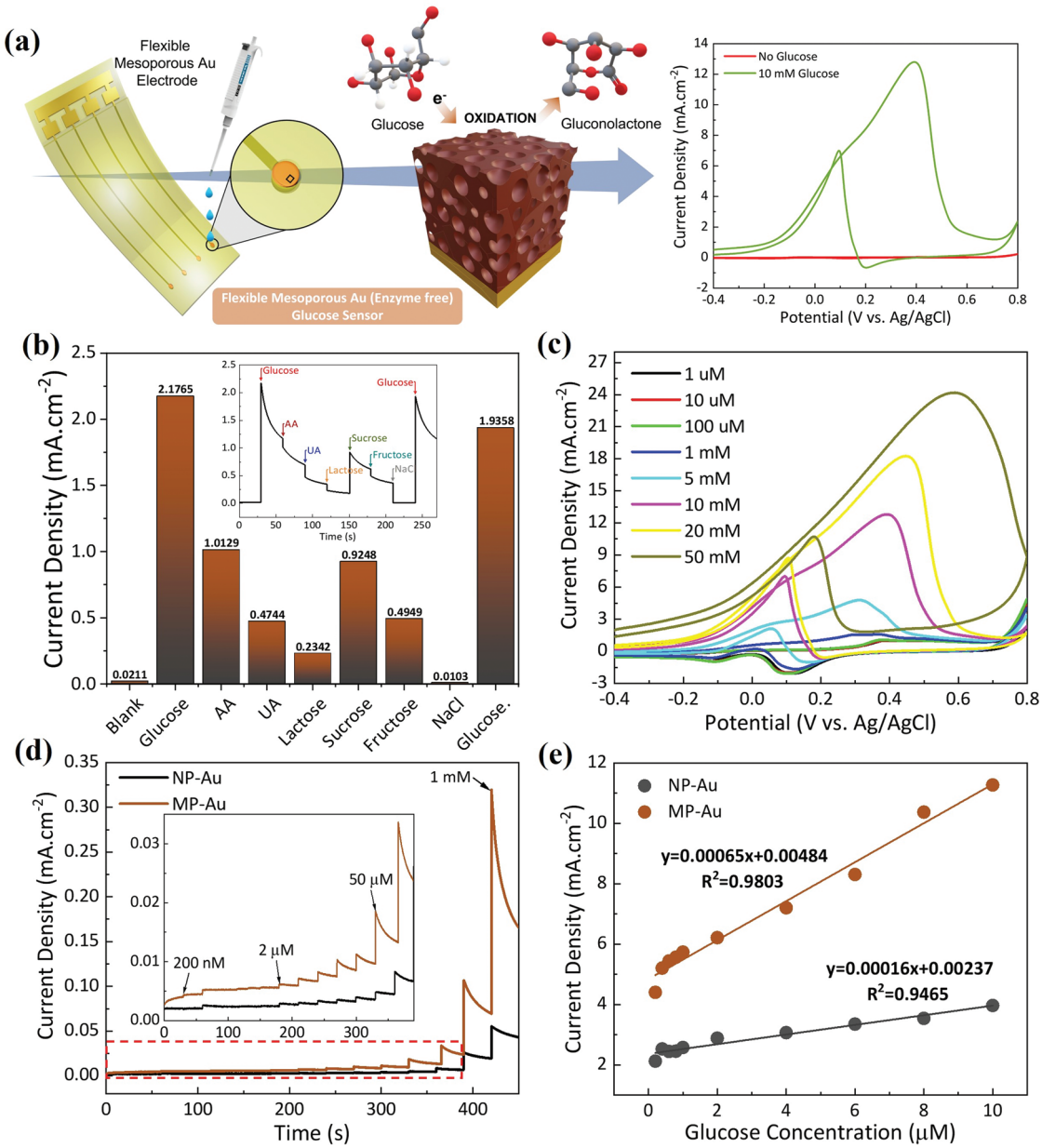

Figure 4. Flexible mesoporous materials for electrochemical sensors. a) Illustration of glucose sensing on NP-Au and flexible MP-Au electrodes. b) Chronoamperometric (*i–t*) responses of flexible MP-Au electrode toward the common interference (10 mM each in PBS) encounter with glucose in bodily fluids. c) CV of glucose oxidation reaction with different concentrations of glucose ranging from 1 μM to 50 mM. d) Successive chronoamperometry curves with glucose concentration from 0.2 to 1 mM. e) The linear relationship (standard curve) of current density versus different concentrations of glucose.

current than the NP-Au counterpart. Furthermore, a high correlation factor of 0.98 in the flexible MP-Au electrodes indicates their excellent linearity with the glucose concentration varying from 200 nM to 10 μM. The limit of detection (LoD) is estimated to be 1.95×10^{-6} M (1.95 μM) with a signal-to-noise ratio of 3 (Figure S11 and Table S1, Supporting Information). This lower LoD demonstrates the high sensitivity of the developed flexible mesoporous platform for biosensing applications (Figure 4e). The flexible MP-Au has higher sensitivity and a lower detection limit than NP–Au and other electrode materials. Moreover, this high level of sensitivity of flexible MP-Au is even higher than that of the flat (or non-flexible) porous Au film (1.95 vs 4.13 μM) (Table S2 and Figure S10, Supporting Information).[41] Therefore, the flexibility and high sensitivity of the MP-Au can be potentially translated to wearable systems for real-time monitoring of body glucose.

The low impedance in flexible MP-Au on PI films (≈1 kΩ at a 1 kHz) and mechanical flexibility suggest their potential for implanted neurophysiological recording applications. We conducted a peripheral nerve *in vivo* recording experiment in the sciatic nerve of a rat model to demonstrate this functionality. Recent findings in the use of electrical stimulation to regain limb control in patients with spinal cord injuries suggested the promise of soft electronics as a neural interface for peripheral nerve stimulation and recording as a route toward the effective treatment of nervous system disorders. To demonstrate

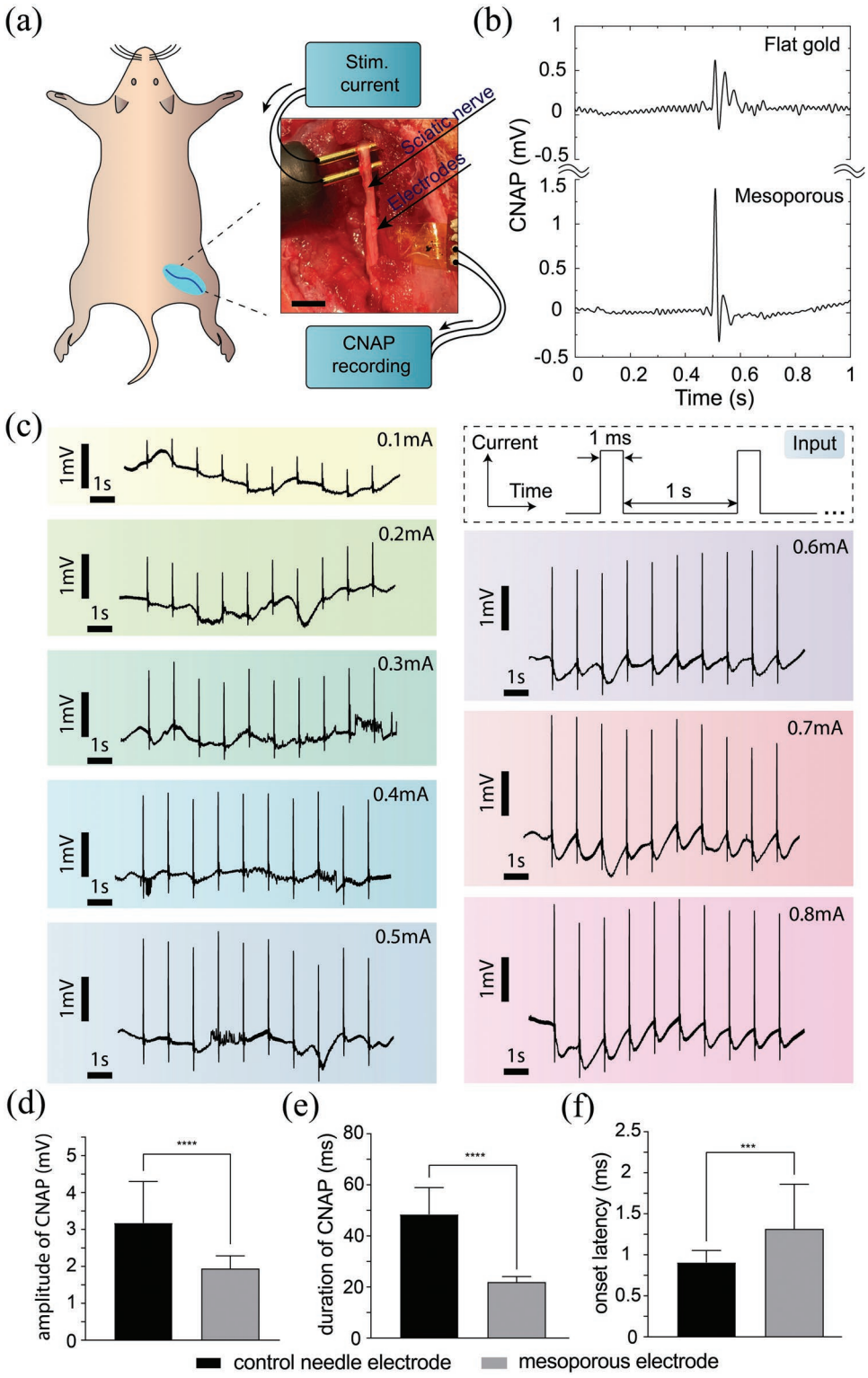

Figure 5. Flexible mesoporous electronics (MP-Au) for in vivo applications. Electrophysiology recording of the rat sciatic nerve: a) schematic sketch of the compound nerve action potential (CNAP) experiment on a rat model, b) comparison of recorded CNAP from mesoporous and flat Au electrodes at a stimulation current of 0.3 mA, c) waveform of CNAP recorded at varying stimulating current from 0.1 to 0.8 mA, comparisons of d) CNAP amplitude, e) CNAP duration, and f) CNAP onset latency between the mesoporous electrode and standard control electrodes.

this functionality, a peripheral nerve *in vivo* recording experiment was conducted in the sciatic nerve of a rat model. A gold bipolar electrode (AD instruments MLA0320) was placed under the sciatic nerve to apply electrical stimuli, **Figure 5**a. The nerve was electrically stimulated using rectangular pulses with a duration of 1.0 ms and a repetition rate of 1 Hz, which were

generated from a standard stimulus isolator (AD instruments FE180). The flexible mesoporous and the flat Au electrode were either connected to the stimulating site of a sciatic nerve to benchmark the electrophysiology recording performance of the mesoporous electrodes. Figure 5b presents the compound nerve action potential (CNAP) recorded using the mesoporous and NP-Au electrodes at a stimulation current of 0.3 mA. Both types of electrodes are able to record CNAP responses such as amplitude, duration, and onset latencies. We compared the signal-to-noise ratio (SNR) of CNAP responses of the flat Au and MP-Au electrodes in the range of stimulation current of 0.1 to 0.8 mA. It can be observed that the SNR of the MP-Au electrodes is increased over 150% compared to flat Au electrodes. This is attributed to the mesoporous electrode's lower impedance because of its greater surface area from the porous microstructure.

Subsequently, the flexible MP-Au electrode was used under varying stimulus current to i) investigate the threshold and supramaximal of the CNAP graded response and to ii) benchmark with a commercial needle electrode at a supramaximal stimulation, as illustrated in Figure 5d–f. Over the repetition of ten stimulus impulses (at the same current), the CNAP signals measured by the flexible MP-Au electrode show a consistent amplitude, indicating good repeatability in physiological recording (Figure 5c). Increasing the stimulus currents leads to an increase in the magnitude of CNAP until the supramaximal was reached at ≈0.8 mA. At this supramaximal current, the recorded mean CNAP amplitude is found to be 1.94 ± 0.3 mV for the flexible MP-Au and 3.17 ± 1.1 mV for the control needle electrode, Figure 5d. The recorded mean CNAP duration from the flexible MP-Au electrode and the control device is found to be 21.9 ± 2.2 and 48.4 ± 10.5 ms, respectively, demonstrating that the control needle electrodes recorded a significantly longer CNAP duration compared to the mesoporous nerve wrap ($P << 0.0001$) as shown in Figure 5e. Finally, the recorded mean CNAP onset latency—which indicates the time from the onset of the stimulation artifact to the onset of the CNAP—for the mesoporous nerve wrap is 1.3 ± 0.5 ms and the control was 0.9 ± 0.1 ms, indicating that the nerve wrap records a significantly slower CNAP onset compared to the control ($p = 0.0008$), Figure 5f. The significant differences in the CNAPs parameters between the two recording systems are likely attributed to the smaller distance separating the anode and cathode within the nerve wrap compared to the control electrodes. The difference in the CNAP signals also indicates that physiological recording highly depends on the relative position, contact of the electrodes and interface with the nerve (e.g., non-invasive for the flexible electrode vs invasive for the needle-type electrode). This is due to the difference between the distance of the cathode and anode electrodes of the control devices and the mesoporous devices. Specifically, the distance between the cathode and anode of the standard needle type electrode is 3000 µm, while that of the mesoporous devices is 750 µm. This leads to a difference in the fundamental parameters of the CNAP signal using different configurations. The results suggest that low-impedance flexible mesoporous electrodes[42] with the ability to form a conformal contact with biological tissue could provide additional functions compared to standard, more invasive needle-type electrodes.

3. Conclusion

In this work, we have established a novel approach for the development of flexible mesoporous architectures employing selective electrochemical deposition on pre-patterned microstructures. Conductive mesoporous nanostructure with metallic framework, which can be fabricated using a soft-templating approach, exhibits excellent mechanical flexibility while maintaining relatively uniform mesoporous networks, with the pore size in a range of 24 nm. Experimental studies on the detection of glucose levels show that the mesoporous electrode offers a high sensitivity of 0.65 mA $cm^{-2}.µM^{-1}$ in the flexible MP-Au platform, which is approximately five times higher than that of NP-Au film based devices. The large surface area of the mesopore networks offer a lower electrochemical impedance of less than 1 kΩ at 1 kHz in microsize electrodes (60 µm in diameter), enabling the detection of compound nerve action potential in rat peripheral nerves. Our novel material systhesis and manufacturing method open up new exciting opportunities in flexible mesoporous materials as an innovative platform for implanted electronics and biological sensing applications.

4. Experimental Section

Fabrication of Micropatterned Electrodes: The micropatterns were transferred onto the flexible PI substrates through a photolithography process using EVG 620 mask aligner. The PI substrates were prepared by spin-coating PI on a poly(methyl methacrylate) (PMMA)-coated silicon wafer at 3000 rpm and thermally annealed for 2 min at 100 °C. This process was repeated until the desired thickness of ≈10 µm was achieved and vacuum annealed at 250 °C. On this, a photomask was exposed to a negative photoresist-coated wafer. 20 nm of Ti and 200 nm of Au were thermally evaporated onto the developed wafer and the remaining photoresist was removed. Finally, another layer of PI was coated on top of the electrodes with dedicated slots exposing the underlying electrode for deposition, Figure S12, Supporting Information.

Electrochemical Deposition of Mesoporous Au on the PI: The mesoporous electrodes used in this study were electrochemically deposited by combining the self-assembled block copolymeric micelle PS-*b*-PEO (Polystyrene-block-polyethylene glycol) using the authors' established protocol.[43] To 10 mg of PS(10k)-*b*-PEO(4.1k) dissolved by stirring in 3 mL of THF (Tetrahydrofuran). Successively, 1 mL of 40 mM $HAuCl_4$ as Au precursor in DI-W (Deionized water) was followed by 1.5 mL of absolute ethanol. Finally, by adding 2.5 mL of DI-W, the Au electrolyte with micelle was set for deposition. The electrochemically processed film was deposited using a three-electrode configuration in a single reaction cell. With Pt gauge and Ag/AgCl as the counter and reference electrodes, the working micropatterned electrode on the PI substrate was immersed into the prepared electrolyte with micelle. By applying –0.5 V for 1000 s, the MP-Au film was deposited on the exposed sites of the working electrode. All electrochemical deposition and characterization were performed in CH Instruments, CHI 660E electrochemical workstation.

Material Characterization: The microstructures of the samples were observed through JEOL JSM-7001F, a field-emission scanning electron microscope (FE-SEM) operated at 15 kV accelerating voltage. The optical properties of both NP–Au and MP-Au electrodes were analyzed in Shimadzu UV-2600 with an integrating sphere. Before the measurement, the beam path was blanked using a PI film to just account for the optical properties of the deposited film in the visible spectrum. The grazing incidence X-ray diffraction (GI-XRD) was performed in an out-of-plane configuration with a Cu Kα sourced to 200 mA at 45 kV in Rigaku SmartLab.

Finite Element Analysis for Supporting Information: Finite element analysis was conducted to predict the stress distribution in Au functional layers during the bending test. Linear buckling analysis was performed, incorporating the initial geometric imperfection condition for post-buckling analysis. Elastic modulus (E) and Poisson ratios (ν) of Au and Pi are given as: E_{Au} = 32 GPA, ν_{Au} = 0.42; E_{PI} = 2.5 GPa, ν_{PI} = 0.34, respectively. It can be seen from the nonlinear bulking simulation that the maximum stress induced onto the top Au layer was estimated to be 220 MPa (Figure S4, Supporting Information), which was well below its Yield stress (300 MPa) and ultimate tensile stress (390 MPa).[44] It was evident that the Au layer would deform within the elastic regime during the bending cycle and maintain its physical and electrical properties. The stiffness of Au/Pi stacking layers was estimated, dominated by the 6 µm PI layer, as: $S = E_{PI} \times t^3/12$, where E_{PI} is elastic modulus, and t is the thickness of the PI film. As such, a stiffness of 4.5×10^{-9} N m^{-1} was obtained, which is 50 times smaller than Si nano ribbons reported in the literature.[45] This demonstrates that the Au/PI platform was highly desirable for flexible and implantable electronics.

Electrochemical Measurement: Prior to any electrochemical analysis, both NP-Au and MP-Au electrodes were cleaned by performing cyclic voltammetry in 0.5 M H_2SO_4 at a higher scan rate. The ECSA for both electrodes were performed at 100 mV s^{-1} in 0.5 M H_2SO_4. For glucose oxidation, cyclic voltammetry were performed using a freshly prepared glucose solution dissolved in 0.1 M NaOH in the potential range of –400 mV to 800 mV. The chronoamperometry (i–t) experiment were conducted using the MP-Au as a working electrode at 100 mVs^{-1}.

Electrophysiology Nerve Recordings: The study was carried out on three Wistar female rats weighing between 320 and 380 g. All the animal procedures were approved by the University's Animal Research Ethics Committee (Protocol number: ENG/01/21/AEC). To maintain consistency, electrophysiology recordings were performed on the right sciatic nerve.[46,47] The rats were anaesthetized with an O_2/Isoflurane mixture (30%/1–2%). Rats were placed prone over a heat blanket and limb stabilization was achieved via adhesive tape. The surgical site was shaved away at the right gluteal region. A skin incision was performed extending from a midpoint (between the hip joint and ischial tuberosity) to the knee. Blunt dissection was carried out (muscle splitting approach) using Iris scissors between the gluteus maximus and biceps femoris muscle. The sciatic nerve was identified under the gluteus maximus muscles. The nerve was isolated from the surrounding connective tissues and fascia using micro-scissors. The epineurium and its blood vessels were preserved.

For the control, the recording was carried out with two active needle electrodes connected to the bioamplifier (AD instruments FE 231) and placed under the sciatic nerve ≈20 mm from the stimulating electrode (Figure S13, Supporting Information). One reference electrode (connected to the bioamplifier) was placed at the distal end of the sacrum. For the mesoporous and non-porous Au electrodes, the recording was carried out with the device wrapped around the circumference of the sciatic nerve, ≈20 mm from the stimulating electrode and connected to the bioamplifier (AD instruments FE 231). One reference electrode (connected to the bioamplifier) was placed at the distal end of the sacrum. Recordings were made and analyzed using PowerLab 4/26 channel recorder and LabChart software (AD instruments).

Statistics: Statistical analysis was performed using Prism 8 (GraphPad Software, San Diego, USA) on data acquired from Wistar female rats (n = 3); amplitude (Figure S14, Supporting Informatio), duration and onset latencies were analyzed with mean ± SD at a sample size of n = 10 supramaximal CNAP responses for both control and mesoporous electrodes; test for normal distribution (normality and lognormality tests) was performed using the Kolmogorov–Smirnov test for normal distribution of the three parameters (amplitude, duration, onset latency) which passed normality test (alpha = 0.05); statistical analysis was then performed using two-tailed paired t-tests between the control and mesoporous electrodes for three parameters (amplitude, duration, onset latency); differences were considered significant at P-value < 0.05.

Supporting Information

Supporting Information is available from the Wiley Online Library or from the author.

Acknowledgements

A.A. and T.-K.N. contributed equally to this work. This study was conducted in part at the Australian National Fabrication Facility, Queensland Node (ANFF-Q), a firm founded under the National Collaborative Research Infrastructure Strategy to offer researchers in Australia with nano- and microfabrication capabilities. The authors further recognise the scientific and technical support provided by the Australian Microscopy and Microanalysis Research Facility at the Centre for Microscopy and Microanalysis, the University of Queensland. A.A. was funded by the UQ's Research and Training Program. Y.Y and Y.V.K acknowledge the research supported by the JST-ERATO Materials Space-Tectonics Project (JPMJER2003) and Advanced Queensland Fellowship (AQIRF043-2020-C). H.P.P acknowledges the research support from the Australian Research Council, Grant ID DE200100238 and the Start-up Grant from the School of Mechanical and Manufacturing Engineering (PS65695), The University of New South Wales, Australia. T.-K.N. acknowledges the support from the Griffith Postdoctoral Fellowship and Griffith IMPACT Spotlight. The author would like the thank the support from the ARC Research Hub for Connected Sensors for Health, which is funded by Australian Research Council (IH210100040).

Open access publishing facilitated by University of New South Wales, as part of the Wiley - University of New South Wales agreement via the Council of Australian University Librarians.

Conflict of Interest

The authors declare no conflict of interest.

Data Availability Statement

The data that support the findings of this study are available from the corresponding author upon reasonable request.

Keywords

biosensors, flexible mesoporous electronics, flexible mesoporous gold electrodes, implanted electronics, physiological monitoring

Received: August 11, 2022
Revised: November 1, 2022
Published online:

[1] T. A. Truong, T.-K. Nguyen, H. Zhao, N.-K. Nguyen, T. Dinh, Y. Park, T. Nguyen, Y. Yamauchi, N.-T. Nguyen, H.-P. Phan, *Small* **2022**, *18*, 2105748.

[2] Y. Liu, J. Li, S. Song, J. Kang, Y. Tsao, S. Chen, V. Mottini, K. McConnell, W. Xu, Y. Q. Zheng, J. B. H. Tok, *Prilozi - Maked. Akad. Nauk. Umet., Odd. Prir.-Mat. Bioteh. Nauki* **2020**, *38*, 1031.

[3] T. I. Kim, J. G. McCall, Y. H. Jung, X. Huang, E. R. Siuda, Y. Li, J. Song, Y. M. Song, H. A. Pao, R.-H. Kim, C. Lu, S. D. Lee, I. S. Song, G. C. Shin, R. Al-Hasani, S. Kim, M. P. Tan, Y. Huang, F. G. Omenetto, J. A. Rogers, M. R. Bruchas, *Science* **2013**, *340*, 211.

[4] Z. Yi, F. Xie, Y. Tian, N. Li, X. Dong, Y. Ma, Y. Huang, Y. Hu, X. Xu, D. Qu, X. Lang, *Adv. Funct. Mater.* **2020**, *30*, 2000477.
[5] S. Abolpour Moshizi, H. Moradi, S. Wu, Z. J. Han, A. Razmjou, M. Asadnia, *Adv Mater* **2022**, *7*, 2100783.
[6] M. Mehrali, S. Bagherifard, M. Akbari, A. Thakur, B. Mirani, M. Mehrali, M. Hasany, G. Orive, P. Das, J. Emneus, T. L. Andresen, D.-P. Alireza, *Adv. Sci.* **2018**, *5*, 1700931.
[7] H. S. Mayberg, A. M. Lozano, V. Voon, H. E. McNeely, D. Seminowicz, C. Hamani, J. M. Schwalb, S. H. Kennedy, *Neuron* **2005**, *45*, 651.
[8] E. Cingolani, J. I. Goldhaber, E. Marbán, *Nat. Rev. Cardiol.* **2018**, *15*, 139.
[9] E. Song, J. Li, S. M. Won, W. Bai, J. A. Rogers, *Nat. Mater.* **2020**, *19*, 590.
[10] H. P. Phan, Y. Zhong, T. K. Nguyen, Y. Park, T. Dinh, E. Song, R. K. Vadivelu, M. K. Masud, J. Li, M. J. A. Shiddiky, D. Dao, Y. Yamauchi, J. A. Rogers, N.-T. Nguyen, *ACS Nano* **2019**, *13*, 11572.
[11] T. A. Pham, T. K. Nguyen, R. K. Vadivelu, T. Dinh, A. Qamar, S. Yadav, Y. Yamauchi, J. A. Rogers, N.-T. Nguyen, H.-P. Phan, *Adv. Funct. Mater.* **2020**, *30*, 2004655.
[12] Y. Cho, S. Park, J. Lee, K. J. Yu, *Adv. Mater.* **2021**, *33*, 2005786.
[13] H. Fang, K. J. Yu, C. Gloschat, Z. Yang, E. Song, C. H. Chiang, J. Zhao, S. M. Won, S. Xu, M. Trumpis, Y. Zhong, S. W. Han, Y. Xue, D. Xu, S. W. Choi, G. Cauwenberghs, M. Kay, Y. Huang, J. Viventi, I. R. Efimov, J. A. Rogers, *Nat. Biomed. Eng.* **2017**, *1*, 0038.
[14] D. Khodagholy, J. N. Gelinas, T. Thesen, W. Doyle, O. Devinsky, G. G. Malliaras, G. Buzsáki, *Nat. Neurosci.* **2015**, *18*, 310.
[15] W. Franks, I. Schenker, P. Schmutz, A. Hierlemann, *IEEE Trans. Biomed. Eng.* **2005**, *52*, 1295.
[16] C. Lim, Y. J. Hong, J. Jung, Y. Shin, S. H. Sunwoo, S. Baik, O. K. Park, S. H. Choi, T. Hyeon, J. H. Kim, S. Lee, *Sci. Adv.* **2021**, *7*, eabd3716.
[17] K. Tybrandt, D. Khodagholy, B. Dielacher, F. Stauffer, A. F. Renz, G. Buzsáki, J. Vörös, *Adv. Mater.* **2018**, *30*, 1706520.
[18] G. Hong, C. M. Lieber, *Nat. Rev. Neurosci.* **2019**, *20*, 330.
[19] T. Leng, X. Huang, K. Chang, J. Chen, M. A. Abdalla, Z. Hu, *IEEE Antennas. Wirel. Propag. Lett.* **2016**, *15*, 1565.
[20] K. Kostarelos, M. Vincent, C. Hebert, J. A. Garrido, *Adv. Mater.* **2017**, *29*, 1700909.
[21] D. Kuzum, H. Takano, E. Shim, J. C. Reed, H. Juul, A. G. Richardson, J. de Vries, H. Bink, M. A. Dichter, T. H. Lucas, D. A. Coulter, E. Cubukcu, *Nat. Commun.* **2014**, *5*, 5259.
[22] Y. Lu, H. Lyu, A. G. Richardson, T. H. Lucas, D. Kuzum, *Sci. Rep.* **2016**, *6*, 33526.
[23] M. Zhang, R. Guo, K. Chen, Y. Wang, J. Niu, Y. Guo, Y. Zhang, Z. Yin, K. Xia, B. Zhou, H. Wang, *Proc. Natl. Acad. Sci. U. S. A.* **2020**, *117*, 14667.
[24] N. V. Apollo, M. I. Maturana, W. Tong, D. A. Nayagam, M. N. Shivdasani, J. Foroughi, G. G. Wallace, S. Prawer, M. R. Ibbotson, D. J. Garrett, *Adv. Funct. Mater.* **2015**, *25*, 3551.
[25] J. W. Seo, K. Kim, K. W. Seo, M. K. Kim, S. Jeong, H. Kim, J. W. Ghim, J. H. Lee, N. Choi, J. Y. Lee, H. J. Lee, *Adv. Funct. Mater.* **2020**, *30*, 2000896.
[26] Z. Xiang, S. C. Yen, S. Sheshadri, J. Wang, S. Lee, Y. H. Liu, L. D. Liao, N. V. Thakor, C. Lee, *Adv. Mater.* **2016**, *28*, 4472.
[27] S. Liu, Y. Zhao, W. Hao, X. D. Zhang, D. Ming, *Biosens. Bioelectron.* **2020**, *170*, 112645.
[28] J. P. Neto, A. Costa, J. Vaz Pinto, A. Marques-Smith, J. C. Costa, R. Martins, E. Fortunato, A. R. Kampff, P. Barquinha, *ACS Appl. Nano Mater.* **2021**, *4*, 5737.
[29] S. Lienemann, J. Zötterman, S. Farnebo, K. Tybrandt, *J. Neural Eng.* **2021**, *18*, 045007.
[30] K. J. Seo, P. Artoni, Y. Qiang, Y. Zhong, X. Han, Z. Shi, W. Yao, M. Fagiolini, H. Fang, *Adv. Biosyst.* **2019**, *3*, 1800276.
[31] T. Qiu, B. Luo, E. M. Akinoglu, J. H. Yun, I. R. Gentle, L. Wang, *Adv. Funct. Mater.* **2020**, *30*, 2002556.
[32] Y. Qiang, P. Artoni, K. J. Seo, S. Culaclii, V. Hogan, X. Zhao, Y. Zhong, X. Han, P. M. Wang, Y. K. Lo, Y. Li, *Sci. Adv.* **2018**, *4*, eaat0626.
[33] C. Zhang, Z. Peng, C. Huang, B. Zhang, C. Xing, H. Chen, H. Cheng, J. Wang, S. Tang, *Nano Energy* **2021**, *81*, 105609.
[34] A. Brahem, A. Al-Hamry, M. A. Gross, L. G. Paterno, M. B. Ali, O. Kanoun, *J. Compos. Sci.* **2022**, *6*, 221.
[35] J. Wang, J. Tang, B. Ding, V. Malgras, Z. Chang, X. Hao, Y. Wang, H. Dou, X. Zhang, Y. Yamauchi, *Nat. Commun.* **2017**, *8*, 15717.
[36] A. Ashok, A. Vasanth, T. Nagaura, M. Eguchi, N. Motta, H.-P. Phan, N.-T. Nguyen, J. G. Shapter, J. Na, Y. Yamauchi, *Angew. Chem., Int. Ed.* **2022**, *61*, e202114729.
[37] T. Nagaura, H.-P. Phan, V. Malgras, T.-A. Pham, H. Lim, A. Ashok, J. Kim, J. You, N.-T. Nguyen, J. Na, Y. Yamauchi, *Angew. Chem., Int. Ed.* **2021**, *60*, 9660.
[38] M. K. Masud, J. Na, T. E. Lin, V. Malgras, A. Preet, A. A. I. Sina, K. Wood, M. Billah, J. Kim, J. You, K. Kani, A. E. Whitten, C. Salomon, N.-T. Nguyen, M. J. A. Shiddiky, M. Trau, M. S. A. Hossain, Y. Yamauchi, *Biosens. Bioelectron.* **2020**, *168*, 112429.
[39] M. K. Masud, M. N. Islam, M. H. Haque, S. Tanaka, V. Gopalan, G. Alici, N.-T. Nguyen, A. K. Lam, M. S. A. Hossain, Y. Yamauchi, M. J. A. Shiddiky, *Chem. Commun.* **2017**, *53*, 8231.
[40] C. Li, Ö. Dag, T. D. Dao, T. Nagao, Y. Sakamoto, T. Kimura, O. Terasaki, Y. Yamauchi, *Nat. Commun.* **2015**, *6*, 6608.
[41] F. Decataldo, T. Cramer, D. Martelli, I. Gualandi, W. S. Korim, S. T. Yao, M. Tessarolo, M. Murgia, E. Scavetta, R. Amici, B. Fraboni, *Sci. Rep.* **2019**, *9*, 10598.
[42] Y. Wyser, C. Pelletier, J. Lange, *Packag. Technol. Sci.* **2001**, *14*, 97.
[43] C. S. A. Gong, W. J. Syu, K. F. Lei, Y. S. Hwang, *Sensors* **2016**, *16*, 1613.
[44] A. S. Nugraha, C. Li, J. Bo, M. Iqbal, S. M. Alshehri, T. Ahamad, V. Malgras, Y. Yamauchi, T. Asahi, *ChemElectroChem* **2017**, *4*, 2571.
[45] C. W. J. M. Kim, Y. K. Kim, J. H. Kim, H. J. Lee, S. W. Han, *Sens. Mater.* **2005**, *17*, 277.
[46] T.-K. Nguyen, M. Barton, A. Ashok, T.-A. Truong, S. Yadav, M. Leitch, T.-V. Nguyen, N. Kashaninejad, T. Dinh, L. Hold, Y. Yamauchi, N.-T. Nguyen, H.-P. Phan, *Proc. Natl. Acad. Sci. U. S. A.* **2022**, *119*, e2203287119.
[47] T.-K. Nguyen, S. Yadav, T.-A. Truong, M. Han, M. Barton, M. Leitch, P. Guzman, T. Dinh, A. Ashok, H. Vu, V. Dau, D. Haasmann, L. Chen, Y. Park, T. N. Do, Y. Yamauchi, J. A. Rogers, N.-T. Nguyen, H.-P. Phan, *ACS Nano* **2022**, *16*, 10890.

NANO MICRO small

Supporting Information

for *Small,* DOI: 10.1002/smll.202204946

Flexible Nanoarchitectonics for Biosensing and Physiological Monitoring Applications

Aditya Ashok, Tuan-Khoa Nguyen, Matthew Barton, Michael Leitch, Mostafa Kamal Masud,* Hyeongyu Park, Thanh-An Truong, Yusuf Valentino Kaneti, Hang Thu Ta, Xiaopeng Li, Kang Liang, Thanh Nho Do, Chun-Hui Wang, Nam-Trung Nguyen, Yusuke Yamauchi,* and Hoang-Phuong Phan**

Supporting Information

Flexible Nanoarchitectonics for Biosensing and Physiological Monitoring Applications

Aditya Ashok,[§] Tuan-Khoa Nguyen,[§] Matthew Barton, Michael Leitch, Mostafa Kamal Masud[*], Hyeongyu Park, Thanh-An Truong, Yusuf Valentino Kaneti, Hang Thu Ta, Xiaopeng Li, Kang Liang, Thanh Nho Do, Chun H. Wang, Nam-Trung Nguyen, Yusuke Yamauchi,[*] and Hoang-Phuong Phan[*]*

[§] *A. Ashok and T.-K. Nguyen contributed equally to this work.*

Correspondence to: k.nguyentuan@griffith.edu.au (TKN); m.masud@uq.edu.au (MKM); y.yamauchi@uq.edu.au (YY); hp.phan@unsw.edu.au (HPP)

Supplementary Figures

Supplementary Tables

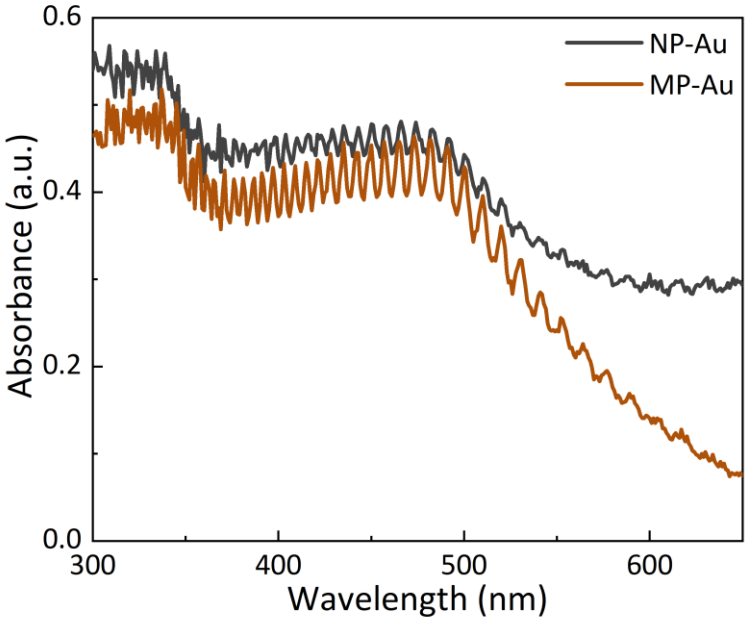

Figure S1. The optical absorbance of NP-Au and MP-Au film on PI as a function of wavelength.

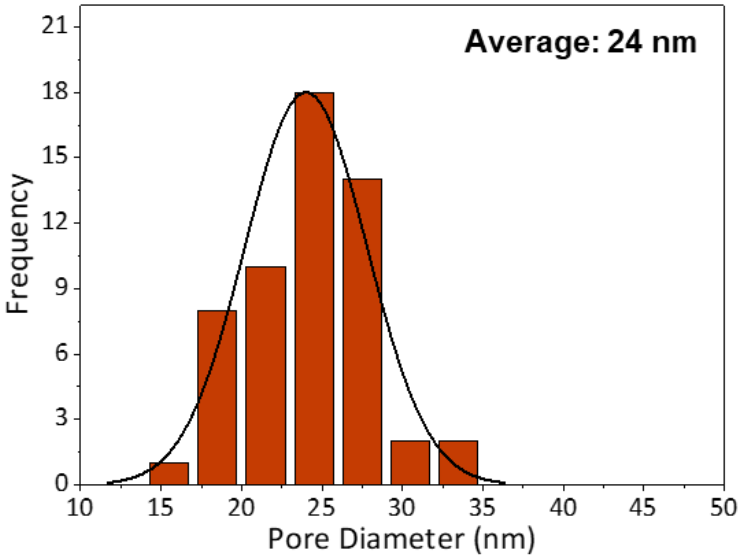

Figure S2. Pore size distribution in MP-Au film on the PI.

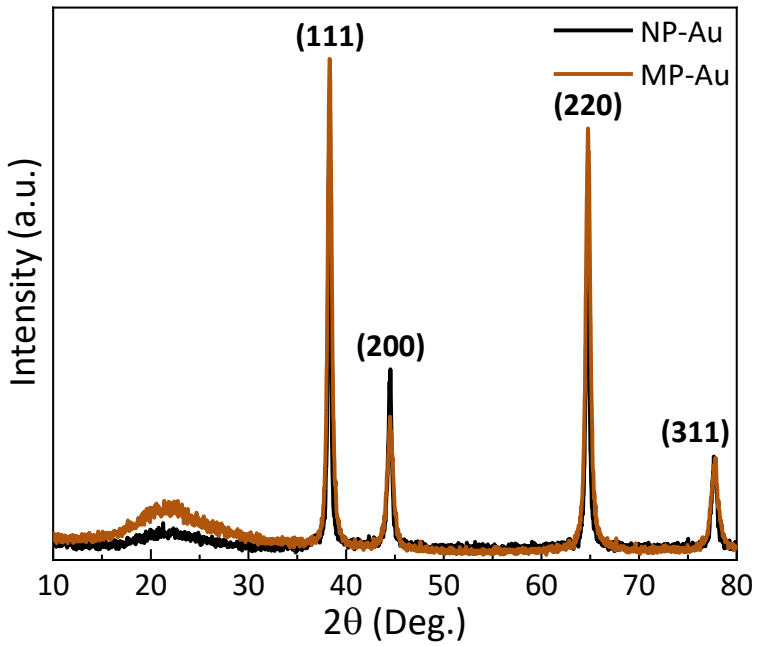

Figure S3. GI-XRD was observed for NP-Au and MP-Au film on the PI.

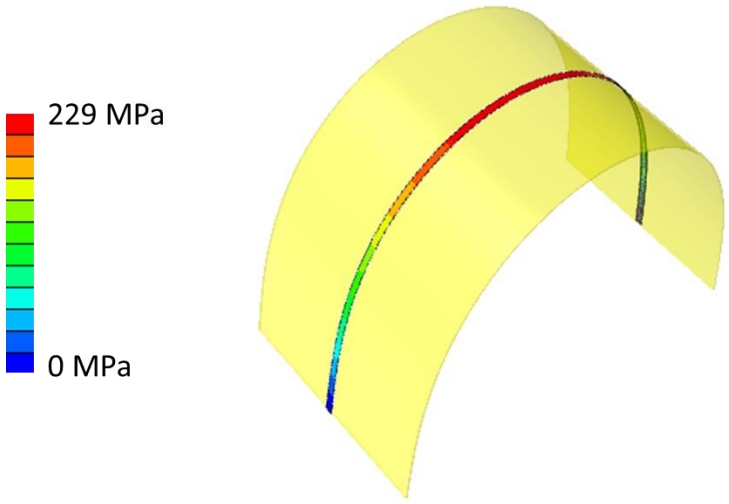

Figure S4. Finite Element Analysis of the strain distribution in Au thin film on PI substrate at a bending curvature of 0.5 mm.

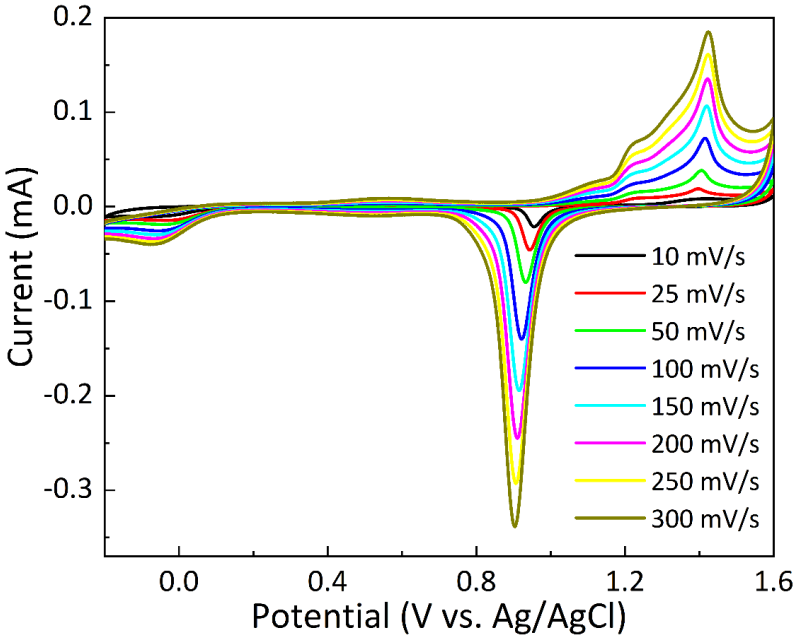

Figure S5. The CV for flexible NP-Au acquired at different scan rates ranging from 10 to 300 mV/s.

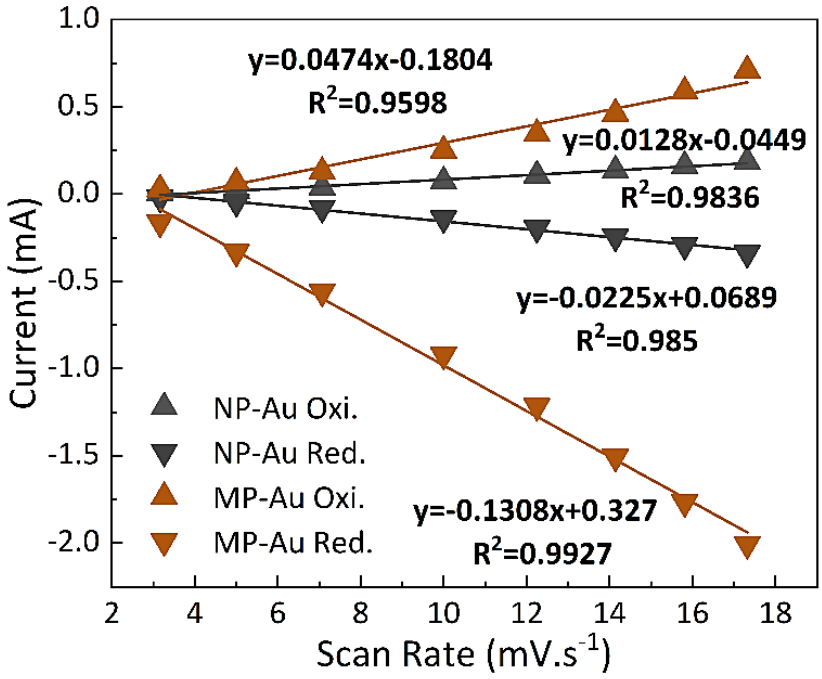

Figure S6. The corresponding curves for anodic (oxi.) and cathodic current (red.) as a function of the square root of scan rate ($v^{1/2}$) range from 10 to 300 mVs^{-1}. The CVs of both MP-Au and NP-Au films were taken in 0.5M H_2SO_4.

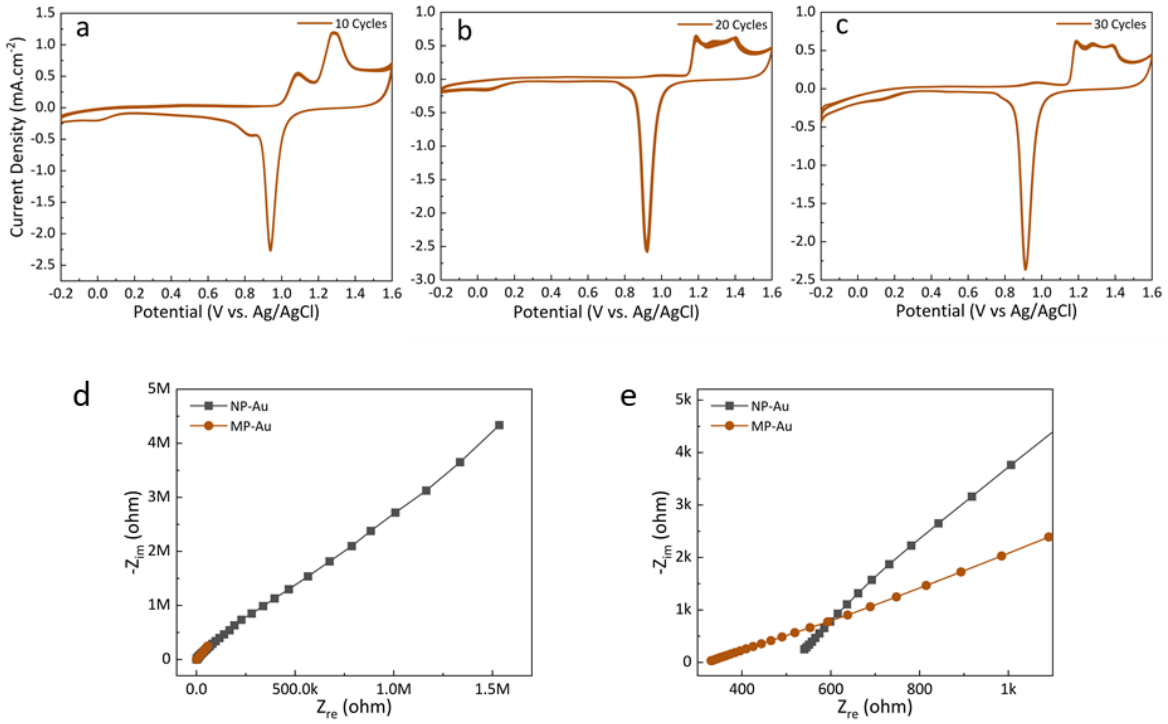

Figure S7. The CVs of MP-Au on multiple cycles: (a) 10 cycles, (b) 20 cycles and (c) 30 cycles in 10 mM PBS (pH 7.0). d) Nyquist plot observed for NP-Au and MP-Au. (e) Nyquist plot magnified at low impedance region indicating the relatively lower series resistance of MP-Au over NP-Au.

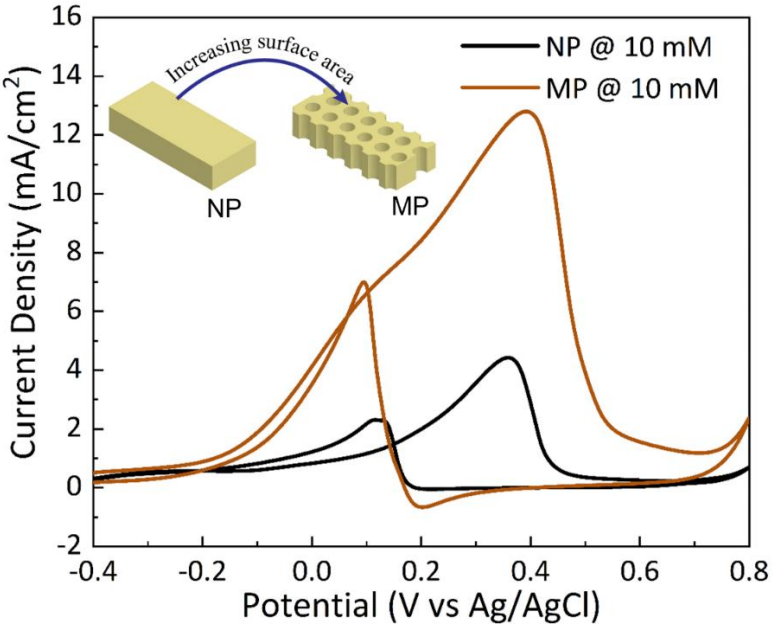

Figure S8. The glucose (10 mM in PBS) oxidation peak for flexible MP-Au and NP-Au.

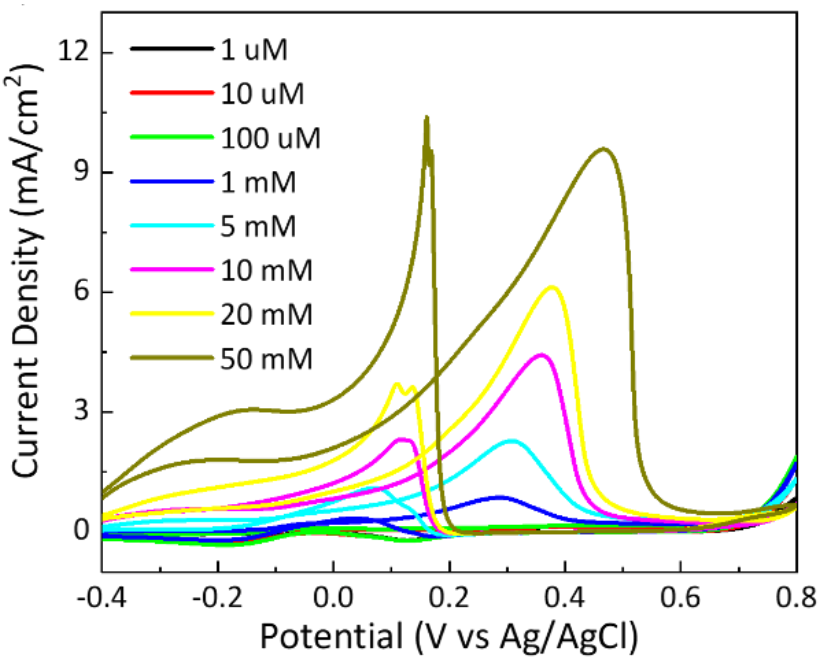

Figure S9. The cyclic voltammetry (glucose oxidation peaks) of NP-Au on the PI for the increasing glucose concentrations.

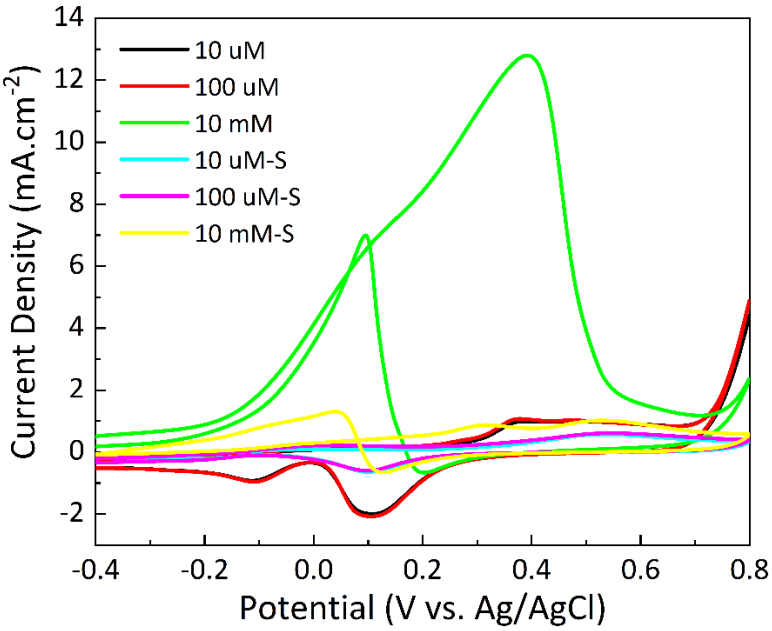

Figure S10. The CV responses of MP-Au for glucose oxidation in PBS and serum (S) sample.

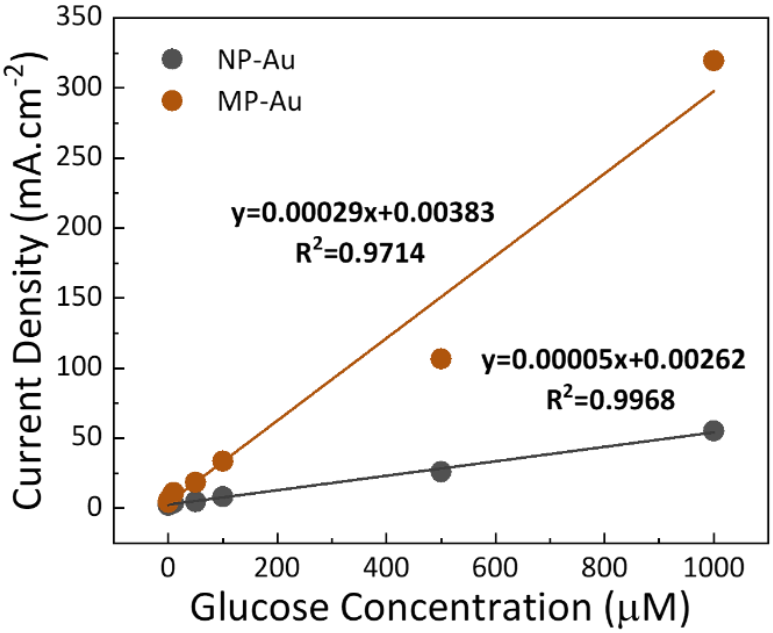

Figure S11. Current density as a function of glucose concentration at all concentrations.

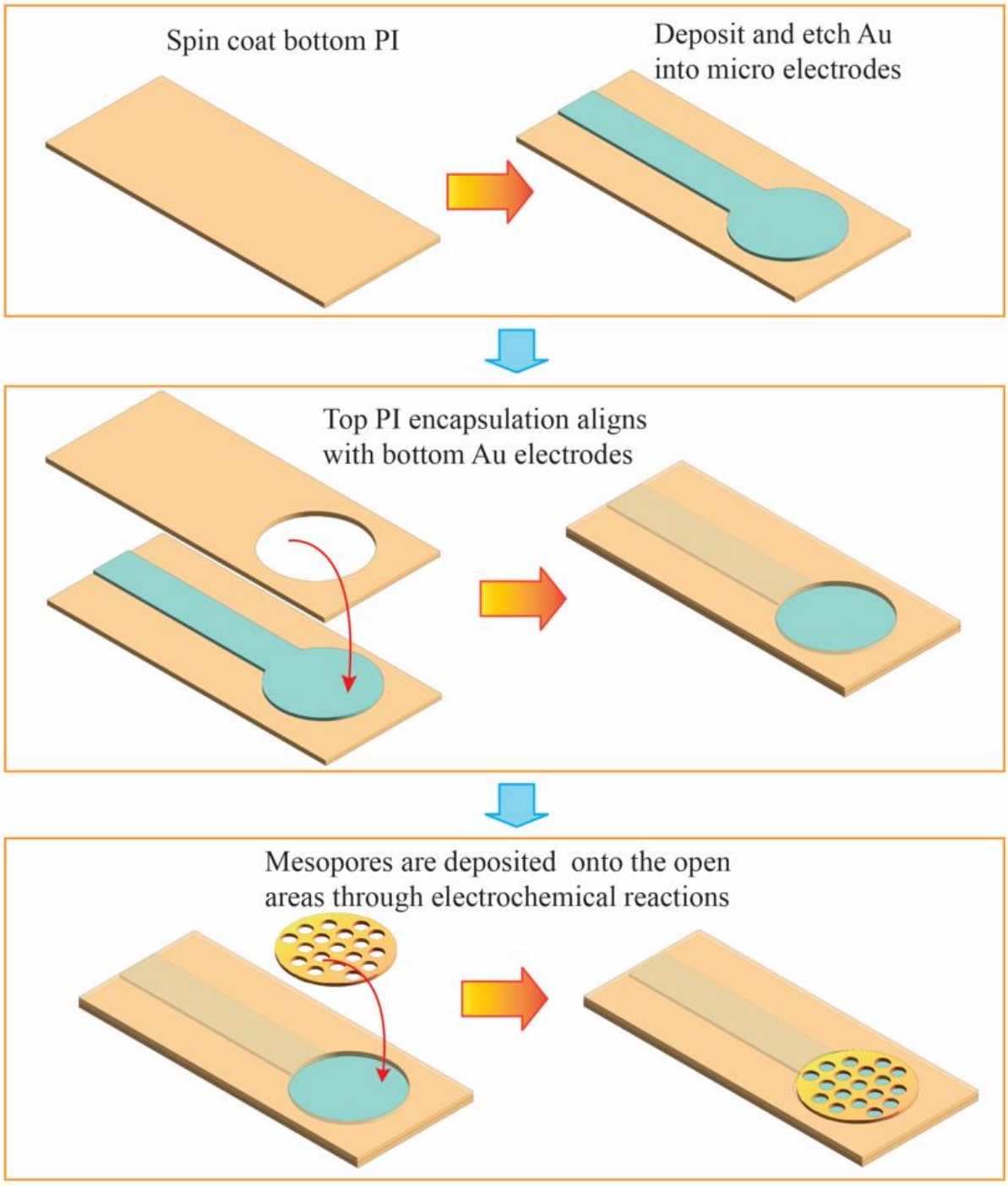

Figure S12. Fabrication process combining top-down lithography and bottom-up electrochemical deposition.

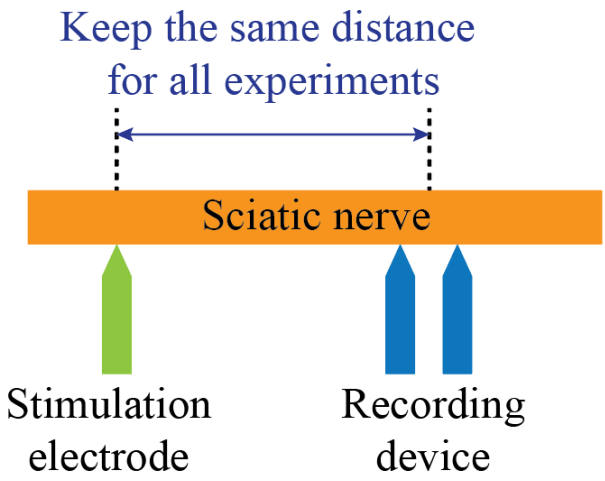

Figure S13. The relative position between the stimulation electrode and the recording device. |The distance between the simulation electrode and recording device was kept at 20mm.

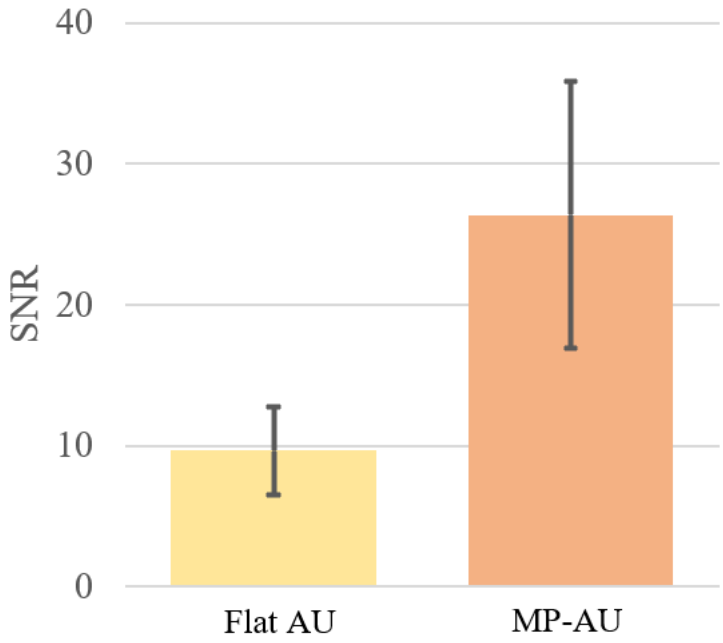

Figure S14. Comparison of average signal-to-noise ratio (SNR) of MP-Au and flat Au electrodes.

Table S1. Limit of Detection (LoD) and sensitivity at a varying concentration of glucose.

LoD (uM)		**Sensitivity ($mA.cm^{-2}.\mu M^{-1}$)**	
NP-Au	MP-Au	NP-Au	MP-Au
8.1555	1.9511	0.15	0.65

Table S2. Comparison of porous Au nanostructures for glucose oxidation (non-enzymatic glucose detection).

Nanomaterials	Synthetic strategy	Non-enzymatic detection of glucose		Advantage	Disadvantage	Ref.
		Linear range	LOD			
Porous Au nanocoral	Dynamic bubble template electrodeposition	0.005 - 13 mM	0.5 μA/mM.cm^2	Simple and single step fabrication procedure	Non-flexible, Required high concentration of basic salt and evolution of H_2	S1
3D hierarchical porous Au networks	Bio-inspired synthesis method, where the natural eggshell membrane (ESM) was introduced as template	1–500 μM	0.2 μM	Green and bio-inspired synthesis. Rigid structure that t free of inactivation caused by aggregation	Non-flexible, involve multi-step procedures, need high temperature (600 ^{o}C) calcination.	S2
Mesoporous carbon–Au NPs	Au NPs were deposited on mesoporous carbon through chemical reduction.	0.05 - 20.0 mM	0.96 μA/mM	This structure provides highly dispersed AuNPs on the outer surface	Need mesoporous carbon for obtaining high activity of Au NPs	S3
Pt-decorated nanoporous Au	NPG was made by dealloying commercial 12-carat white gold membrane in concentrated nitric acid followed by electrodeposition of Pt thin layer	-	-	Porous bimetallic nanostructure exhibits considerable activity toward this reaction in neutral and alkaline solutions	Hard substrate, multi-step procedure involving tedious dealloying and chemical reduction.	S4
Nanoporous Au film	Electrochemical dealloying of Sn component from AuSn alloy, anodic electrodissolution, disproportion and deposition of Au.	2 μM - 8.11 mM	0.36 μM	Rapid fabrication (90s)	Hard substrate, tedious dealloying combined with electro-dissolutions.	S5
Dendrite Au nanostructures	Electrochemical deposition	10.0 μM - 15.0 mM	0.6 μM	Paper substrate, fast electrodeposition that preserve porosity of paper.	Non-porous, single use substrate.	S6
Nanoporous Au	One-step square-wave oxidation reduction cycle	2 μM - 15 mM	0.5 μM	3D nanostructure, rapid and biocompatible.	Hard substrate, need multiple cleaning and deposition steps.	S7
AuNPs)/polyaniline (PANI)/carbon cloth integrated electrode	Au electrochemically polymerized on PANI-modified carbon cloth.	10.26 μM - 10.0 mM	3.08 μM	Flexible and highly conductive and stable.	Multi-step preparations	S8
Flexible mesoporous Au	Mesoporus Au is electrodeposited on a flexible substrate using block polymer as a pore directing agent.	1 μM - 50 mM	1.95 μM	Highly ordered and porous nanostructure. Robust, stable and easy fabrication.	-	This work

References

S1. G. Sanzó, I. Taurino, R. Antiochia, L. Gorton, G. Favero, F. Mazzei, G. De Micheli, S. Carrara, *Bioelectrochemistry*, **2016**, 112, 125-131.

S2. S.L. Zhong, J. Zhuang, D.P. Yang, D. Tang, *Biosens. Bioelectron.* **2017**, 96, 26-32.

S3. L. Wang, J. Bai, X. Bo, X. Zhang, L. Guo, *Talanta*, **2011**, 83, 1386-1391.

S4. X. Yan, X. Ge, S. Cui, *Nanoscale Res. Lett.* **2011**, 6, 1-6.

S5. Y. Pei, M. Hu, F. Tu, X. Tang, W. Huang, S. Chen, Z. Li, Y. Xia, *Biosens. Bioelectron.* **2018**, 117, 758-765.

S6. E. Rafatmah, B. Hemmateenejad, *Sens. Actuators B: Chem.* **2020**, 304, 127335.

S7. G.X. Zhong, W.X. Zhang, Y.M. Sun, Y.Q. Wei, Y. Lei, H.P. Peng, A.L. Liu, Y.Z. Chen, X.H. Lin, *Sens. Actuators B: Chem.* **2015**, 212, 72-77.

S8. M. Xu, Y. Song, Y. Ye, C. Gong, Y. Shen, L. Wang, L. Wang, *Sens. Actuators B: Chem.* **2017**, 252, 1187-1193.